Seismic Moment Tensor Inversion Using 3D Velocity Model and Its Application to the 2013 Lushan Earthquake Sequence

Lupei Zhu[a,b,*], Xiaofeng Zhou[c]

[a]Subsurface Multi-scale Imaging Key Laboratory of Hubei Province, Institute of Geophysics and Geomatics, China University of Geosciences, Wuhan, China
[b]Department of Earth and Atmospheric Sciences, Saint Louis University, St. Louis, MO 63108, USA
[c]Institute of Geophysics, China Earthquake Administration Beijing, China

Abstract

Source inversion of small-magnitude events such as aftershocks or mine collapses requires use of relatively high frequency seismic waveforms which are strongly affected by small-scale heterogeneities in the crust. In this study, we developed a new inversion method called gCAP3D for determining general moment tensor of a seismic source using Green's functions of 3D models. It inherits the advantageous features of the "Cut-and-Paste" (CAP) method to break a full seismogram into the *Pnl* and surface-wave segments and to allow time shift between observed and predicted waveforms. It uses grid search for 5 source parameters (relative strengths of the isotropic and compensated-linear-vector-dipole components and the strike, dip, and rake of the double-couple component) that minimize the waveform misfit. The scalar moment is estimated using the ratio of L_2 norms of the data and synthetics. Focal

[*]Corresponding author; 3642 Lindell Blvd, St Louis, MO 63108, USA. Tel: +01-314-977-3118
  Email address: `zhul@slu.edu` (Xiaofeng Zhou)

depth can also be determined by repeating the inversion at different depths. We applied gCAP3D to the 2013 M_s 7.0 Lushan earthquake and its aftershocks using a 3D crustal-upper mantle velocity model derived from ambient noise tomography in the region. We first relocated the events using the double-difference method. We then used the finite-differences method and reciprocity principle to calculate Green's functions of the 3D model for 20 permanent broadband seismic stations within 200 km from the source region. We obtained moment tensors of the mainshock and 74 aftershocks ranging from M_w 5.2 to 3.4. The results show that the Lushan earthquake is a reverse faulting at a depth of 13–15 km on a plane dipping 40–47° to N46°W. Most of the aftershocks occurred off the main rupture plane and have similar focal mechanisms to the mainshock's, except in the proximity of the mainshock where the aftershocks' focal mechanisms display some variations.

Keywords: Seismic moment tensor inversion, 3D Green's function, 2013 Lushan earthquake.

1. Introduction

An important task in seismology is to determine moment tensor of a seismic event using seismic observations. This 3×3 symmetric tensor with six independent components is defined as the integral of the "stress glut" over the source volume (e.g. Dahlen and Tromp, 1998). It provides fundamental information on the event magnitude, source geometry (e.g., possible fault plane orientations and slip directions), and partition among various deviatoric and isotropic components (e.g. Julian et al., 1998; Chapman and Leaney, 2012; Tape and Tape, 2012; Zhu and Ben-Zion, 2013; Vavrycuk,

2015). Mathematically, the seismic moment tensor is linearly proportional to ground displacement and therefore can be obtained by a linear inversion of observed seismograms, assuming that the Earth structure and the location of the event are known accurately. In practice errors and uncertainties in velocity model and event location need to be taken into account. One critical condition for a reliable moment tensor solution by waveform inversion is that the arrival times of observed and predicted waveforms agree within a fraction of a cycle (Ekstrom et al., 2012). For this reason, most moment tensor inversions that use 1D Earth models for efficient forward calculation are done to low-pass-filtered seismograms. For example, the Global Centroid Moment Tensor (GCMT) project uses long-period (>40 s) body waves and surface waves. Theoretical seismograms are computed using normal modes of a 1D Earth model, with corrections to surface wave dispersion for lateral heterogeneity based on a tomographic whole-mantle model (Ekstrom et al., 2012). It works well for earthquakes larger than magnitude 5.5 globally. Hjorleifsdottir and Ekstrom (2010) assessed effects of 3D Earth structure on GCMT solutions using synthetic data and found only small errors on average in the scalar moment and tensor elements, though the centroid depths and times were biased. However, 3D effects become severe for moment tensor determination of moderate and small earthquakes for which higher frequency waveforms in regional distances are used for better signal-to-noise ratio (Kuhn and Vavrycuk, 2013). Covellone and Savage (2012) compared moment-tensor solutions of 195 M_w >5.5 earthquakes in the Middle East between 1D and 3D inversions. At periods of 25–125 s, 3D inversion reduced error of the solutions. More importantly, using 3D velocity model increased

3

the percentage of double-couple (DC) components, which suggests that the percentage of non-DC components was a result of poorly constrained Earth structure.

To reduce the dependence of seismic source inversion on velocity model and source location, Zhao and Helmberger (1994) developed a "Cut-and-Paste" (CAP) method that breaks a regional seismogram into the Pnl and surface wave segments and allows time shift between observed and predicted waveforms. It uses a grid search of strike and dip of the fault plane and slip direction for the best focal mechanism that minimizes the misfit of observed and predicted seismograms, after the later is time shifted by cross-correlating with the observed waveform. The focal depth is determined by repeating CAP at different source depths. Although 1D velocity models are used in CAP, it has been shown to be robust and reliable for earthquakes down to magnitude 3.5 using regional waveform data up to 0.5 Hz (e.g. Zhu and Helmberger, 1996; Zhu et al., 2006). Tan and Helmberger (2007) added a station-specified amplitude amplification factor (AAF) to CAP and extended earthquake magnitudes to 2 by inverting short-period (0.5–2 Hz) P waveforms. The time shifting has also been adopted in several moment tensor inversion methods that use 1D (e.g. Dreger, 2003) or 3D velocity models (e.g. Ramos-Martinez and McMechan, 2001; Liu et al., 2004; Hingee et al., 2011).

There have been several improvements to CAP in addition to AAF. Zhu and Helmberger (1996) removed the normalization in the waveform misfit definition of original CAP using distance-decay-corrected true amplitudes in order to better preserve the information of source radiation pattern and Pnl/surface wave amplitude ratio which is critical for constraining the focal

depth. Tan et al. (2006) added a grid search for epicenter to relocate earthquakes (CAPloc). Chen et al. (2015) used teleseismic waveforms in CAP (CAPtele) and combined teleseismic and regional seismograms (CAPjoint). Zhu and Ben-Zion (2013) proposed a new parameterization of seismic moment tensor and added grid search for the isotropic and compensated linear vector dipole (CLVD) components in a general moment tensor (gCAP). Despite these progresses, Green's functions of 1D velocity models are still used. CAP works fine in regions with moderate lateral structure variation because the time shifts absorb travel time anomalies of Pnl and surface waves. But 3D velocity models are desired for regions with strong lateral variation, such as at the boundaries of plates and tectonic blocks.

In this paper, we introduce a upgrade to CAP named gCAP3D that uses Green's functions of 3D velocity models to determine a seismic source's general moment tensor. Compared with other 3D velocity model moment tensor inversion methods that use whole seismograms and are thus dominated by the large-amplitude surface waves, gCAP3D inherits the unique feature of CAP of breaking the seismogram into the Pnl and surface wave segments. This allows to apply a higher band-pass filter and to increase the weight to the Pnl waveform which is more stable and less influenced by upper crustal heterogeneities than the surface waves (Zhao and Helmberger, 1994). The amplitude ratio of Pnl and surface wave provides better constrain on the source depth (Zhu and Helmberger, 1996; Zhu et al., 1997). We will apply gCAP3D to the 2013 Lushan M_s 7.0 earthquake in China and its aftershocks. The study area is located at the boundary between the Tibetan plateau and Sichuan Basin where crustal and upper mantle structure exhibits strong lat-

5

Figure 1: Map showing the epicenter (the star) of the 2013 M_s 7.0 Lushan earthquake that occurred at the boundary between the Tibetan plateau and Sichuan Basin in China. Triangles are permanent broadband seismic stations within 200 km from the source region.

eral variation (Fig. 1) and thus provides an idea testing ground for gCAP3D.

2. Method

Let $u(t)$ be a segment of observed seismogram (e.g., Pnl, Rayleigh surface wave, or Love surface wave) with the instrument response removed and $s(t)$ be the corresponding synthetic seismogram that matches the observation with a time shift Δt (due to imperfect velocity model or error in the source location),

$$u(t) = M_0 s(t - \Delta t), \qquad t_1 \leq t \leq t_2, \tag{1}$$

where M_0 is the scalar moment of the source. $s(t)$ is a linear combination of the Green's function $G_{ij}(t)$ from the source to the receiver,

$$s(t) = D_{ij}G_{ij}(t) * S(t). \tag{2}$$

$S(t)$ is the source time function and D_{ij} is the "normalized" moment tensor of the source (i.e., $\mathbf{D} : \mathbf{D} = 2$). It can be decomposed into an isotropic (ISO) tensor, a DC tensor, and a CLVD tensor (Zhu and Ben-Zion, 2013),

$$D_{ij} = \zeta D_{ij}^{\text{ISO}} + \sqrt{1 - \zeta^2} \left(\sqrt{1 - \chi^2} D_{ij}^{\text{DC}} + \chi D_{ij}^{\text{CLVD}} \right), \tag{3}$$

where

$$D_{ij}^{\text{ISO}} = \sqrt{\frac{2}{3}}\delta_{ij}, \tag{4}$$

$$D_{ij}^{\text{DC}} = n_i v_j + v_i n_j, \tag{5}$$

$$D_{ij}^{\text{CLVD}} = \frac{1}{\sqrt{3}}(2b_i b_j - v_i v_j - n_i n_j), \tag{6}$$

where $\hat{\text{n}}$ is the fault normal vector (determined by the strike ϕ and dip δ of the fault plane), $\hat{\text{v}}$ is the slip direction vector (determined by the rake λ), and $\hat{\text{b}} = \hat{\text{n}} \times \hat{\text{v}}$ is the null vector. ζ and χ are non-dimensional parameters quantifying the strength of isotropic and CLVD components, respectively.

$$|\zeta| \leq 1, \tag{7}$$

$$|\chi| \leq 1/2. \tag{8}$$

CAP uses a grid search to solve Eq. (1) for DC source parameters ϕ, δ, and λ (Zhao and Helmberger, 1994). For each possible set of DC source parameters, it first finds Δt by cross-correlating $u(t)$ and $s(t)$ and estimates the scalar moment,

$$M_0 = \frac{\|u\|}{\|s\|}, \tag{9}$$

where $\|\|$ denotes the L_2 norm. It then calculates the waveform misfit e using the L_2 norm of the difference between observed and predicted waveform,

$$e = \|u(t) - M_0 s(t - \Delta t)\|^2. \tag{10}$$

The best DC source parameters are found that minimize e. The procedure is

usually repeated at different source depths to find the optimal focal depth.

CAP uses 5 waveform segments from three-component seismogram of a station: the *Pnl* wave (vertical and radial components), the Rayleigh surface wave (vertical and radial components), and the Love surface wave (the transverse component). Stations at different epicentral distances r_i are usually used. The total waveform misfit is the sum of misfits of all waveform segments used, after correcting for amplitude decay due to geometrical spreading (Zhu and Helmberger, 1996),

$$
\begin{aligned}
E = \sum_{i=1}^{N_s} \Bigg(& w^2 \left(\frac{r_i}{r_0} \right)^2 \left(e_i^{PnlZ} + e_i^{PnlR} \right) \\
& + \frac{r_i}{r_0} \left(e_i^{RaylZ} + e_i^{RaylR} + e_i^{Love} \right) \Bigg),
\end{aligned}
\tag{11}
$$

where r_0 is a reference distance and w is the weight to the *Pnl* wave segment.

The uncertainties of source parameters

$$
\mathbf{m} = (\zeta, \chi, \phi, \delta, \lambda)^{\mathrm{T}},
\tag{12}
$$

can be estimated using the "flatness" of the misfit E at the minimum. We first estimate the *posteriori* data variance (Bevington and Robinson, 1992),

$$
\sigma_d^2 = \frac{E_{\min}}{N_d - M},
\tag{13}
$$

where N_d is the total number of "data points" and M is the number of unknown parameters (e.g., 6 for the moment tensor plus total number of time shifts). Since an individual sample on a seismogram strongly correlates

8

with its neighbors, we count every duration of the dominant period as one independent data point. The covariance matrix of source parameters is

$$C_{ij} = \sigma_d^2 \left[\frac{\partial^2 E}{\partial m_i \partial m_j} \right]^{-1}. \tag{14}$$

3. Application to the 2013 Lushan earthquake and its aftershocks

The 04/20/2013 M_s 7.0 Lushan earthquake occurred in the southern part of the Longmenshan fault zone which marks the boundary between the high-rise Tibetan plateau and low-land Sichuan Basin (Fig. 1). The collision between India and Tibet and the outward growth of the Tibetan plateau thrust the Longmenshan Mts. on top of the rigid Sichuan block. It is the largest earthquake in the fault zone following the 2008 M_s 8.0 Wenchuan earthquake which ruptured ∼300 km of the Longmenshan fault. 196 deaths and more than 10,000 casualties were caused by the Lushan earthquake.

The area is part of the so-called "North-South Seismic Belt" in China and has been well instrumented by permanent seismic stations (Fig. 1). The Lushan earthquake and its aftershocks were recorded by more than 20 broadband three-component seismic stations within 200 km with excellent azimuthal coverage (Fig. 1). The DC moment tensors of the mainshock and large aftershocks were determined by using these regional waveform data and CAP (Lu et al., 2013; Zeng et al., 2013b). Xie et al. (2013) and Han et al. (2014) combined regional and teleseismic waveform data and used CAPtele as well as CAPjoint to determine the mainshock focal mechanism and depth. 1D velocity models were used in all these studies. Lin et al. (2013) obtained moment tensor of the mainshock and 16 aftershocks using time domain mo-

Figure 2: Shear-wave velocity variation at different depths of the 3D crustal-upper mantle model used in this study.

ment tensor inversion TDMT_INV of Dreger (2003). They used three 1D models for stations located in different geologic provinces (i.e., plateau and basin).

Here we used a recent 3D crustal-upper mantle velocity model derived from dispersions of Rayleigh wave phase and group velocities and receiver functions (Zheng et al., 2013). The model extends down to 150 km depth and has a lateral resolution of 50–80 km. S-wave velocity variations of the model at 5, 10, 20, and 50 km are shown in Fig. 2. Strong lateral velocity variation can be seen across the Longmenshan Fault Zone from the surface down to the lower crust and upper mantle.

We collected waveform data of the mainshock and 90 aftershocks in the following two weeks recorded by 20 broadband stations (Fig. 1), provided by Data Management Centre of China National Seismic Network at Institute of Geophysics, China Earthquake Administration (Zheng et al., 2010). We first relocated these events using their differential arrival times measured by waveform cross-correlation and the double-difference method (Waldhauser and Ellsworth, 2000). We then used a staggered-grid 4th-order finite-differences (FD) method (Graves, 1996) to calculate Green's functions of the 3D model. The 450 km×450 km×150 km crustal-upper mantle volume of the study area is divided into 1-km-spacing grid, which sets the maximum frequency of the Green's functions to be 0.4 Hz. Since the number of source grids is more than the number of receivers, we used the reciprocity principle and initialized the FD source at the receiver. Only three FD runs were needed to obtain 18-

component Green's functions for each station to all source grids (Zhao et al., 2006). For comparison, we also calculated 1D Green's functions of different epicentral distances and source depths using the FK method (Zhu and Rivera, 2002) and a 1D model of the study area developed by Zhao et al. (1997).

We band-pass filtered the Pnl waveforms between 0.03 and 0.3 Hz and surface waves between 0.02 and 0.1 Hz. The two segments were given equal weights in the gCAP3D inversion. For the mainshock, we excluded close stations of epicentral distances less than 100 km so that the point-source approximation used in the inversion is valid. We tried triangle-shaped source time functions of different durations and found that a 4-s source duration yielded the minimum misfit. For all aftershocks, since the largest one is less than M_L 5.5 and waveforms were low-pass filtered at 3 s which is longer than the duration of the source, an impulse source time function was used. We also restricted that the moment tensors to DC only.

The moment tensor solutions of the mainshock using the 1D and 3D models are summarized in Table 1 along with other published results. Here we added the double-couple source constraint. Their waveform fits are shown in Fig. 3 and 4, respectively. Although the data variance reduction of 68% using the 3D model seems only slightly better than using the 1D model (64%), the improvements to waveform fits are evident, particularly to the Rayleigh surface waves at all stations. The time shifts needed to align data and synthetics are also reduced (e.g., at stations JLO, DFU, MEK, etc). The ratio of waveform misfits between using the 3D model and 1D model is F=1.12. We used F-test and found that the decrease in misfit by the 3D

Table 1: Moment tensor solutions of the Lushan mainshock using 1D and 3D velocity models with the double-couple constraint (1D and 3D) and using the 3D model with full moment tensor inversion (3Df).

Name	ϕ	δ	λ	M_w	h	ζ	χ
1D	223±2	37±4	101±6	6.4	15	-	-
3D	224±2	41±4	90±6	6.5	13	-	-
3Df	222±2	42±1	90±2	6.5	13	0.28±0.05	-0.13±0.03
GCMT[a]	212	42	100	6.6	22	-	0.10
CAP[b]	210	47	97	6.7	12	-	-
CAPjoint[c]	210	44	91	6.7	16	-	-
TDMT[d]	216	47	101	6.5	13	-	0.01

ϕ, δ, and λ are in degrees. h is in km.
a: www.globalcmt.org; b: Han et al. (2014); c: Xie et al. (2013); d: Lin et al. (2013).

model is significant at 92% confidence level.

We also did full moment-tensor inversion using the 3D velocity model (Table 1). Similar fault plane solutions were obtained but with appreciable isotropic (ζ=0.28) and CLVD (χ=-0.13) components, corresponding to 7.8% and 1.6% of total moment square, respectively. The variance reduction of 71% of full moment-tensor inversion is noticeably better than with the double-couple constraint (68%). Given the deep depth of the earthquake (13–16 km), we believe that it is unlikely for the Lushan earthquake to have such amount of non-double couple components, especially the isotropic component. We found that most of the improvements to the waveform fits by the full-moment inversion are in the transverse components of seismograms. So it is possible that some of the anisotropic velocity structure not represented in the 3D isotropic model were mapped to isotropic and CLVD components of the source.

We used gCAP3D and determined moment tensors of 74 aftershocks (16

Figure 3: Inversion result and waveform fits of the mainshock using the 1D velocity model. Stations are arranged by its epicentral distance (shown in km below the station name). Black traces are observed waveforms and red traces are predicted waveforms. The numbers below each waveform segment are time shift in s. and waveform cross-correlation coefficient in percentage.

Figure 4: Inversion result and waveform fits of the mainshock using the 3D velocity model, see caption of Fig. 3 for details.

Figure 5: Inversion result and waveform fits of a M_w 3.4 aftershock using the 3D velocity model, see caption of Fig. 3 for details.

aftershocks were discarded due to high noise level in their waveform records), ranging from M_w 5.2 to 3.4. Fig. 5 shows waveform fits for the smallest aftershock. Excellent waveform match can be seen for 10-s Rayleigh surface waves at stations up to ∼120 km, while the Pnl waveforms at 3 s and longer are noisy beyond 90 km. Moment tensor solutions of these aftershocks are presented along with the mainshock in Fig. 6. Most of the aftershocks occurred off the main rupture plane and have focal mechanisms similar to the pure thrust faulting of mainshock's with one fault plane dipping about 40° to the NW (Fig. 7). The strike of the plane (224°) agrees with the trend of the Longmenshan fault zone and the thrusting focal mechanisms are consistent with the horizontal shortening stress environment generated by the collision between the Tibetan plateau and Sichuan Block. There are a dozen of aftershocks in the proximity of the mainshock whose focal mechanisms display some variations, including one strike slip faulting and several reverse faulting on either high-angle or sub-horizontal plane.

Figure 6: Focal mechanisms of the mainshock and 74 aftershocks obtained using the 3D velocity model. The bottom panel shows two SE-NW cross-sections perpendicular to the strike of the mainshock fault plane. The black line represents the projection of main rupture plane in the cross sections.

Figure 7: Stereographic project of P and T axes of focal mechanisms of 74 aftershocks. The P and T axes of the mainshock focal mechanism are indicated by the letters P and T, respectively.

4. Discussion and Conclusions

When studying seismic sources of small magnitudes such as aftershocks or mine collapses it is necessary to apply moment-tensor inversions to waveforms of relatively high frequencies at which the signals are strong (e.g. Kuhn and Vavrycuk, 2013). Here we obtained moment tensor of 75 events of the 2013 Lushan earthquake sequence in the first two weeks following the mainshock. Using essentially the same dataset, Lin et al. (2013) determined moment tensors of 17 events by the TDMT_INV method and Lu et al. (2013) obtained moment tensors of 36 events by the CAP method. A critical parameter in these studies is the highest frequency of waveforms used: 0.05 Hz in Lin et al. (2013), 0.2 Hz in Lu et al. (2013), and 0.3 Hz in this study. At high frequencies seismic waves are strongly affected by small-scale heterogeneities in the crust, especially in the shallow part and block boundaries. With recent advancements in seismic tomography using travel-time and ambient noise data of dense arrays, high-resolution 3D Earth models will become available in various areas. A generalized moment tensor inversion using 3D Green's functions such as gCAP3D will find more applications to study seismic sources of tectonic, volcanic, and man-made events.

Overall, our moment tensor solution of the 2013 Lushan earthquake using

3D Green's functions at regional distances is similar to those based regional and teleseismic waveforms (Tab. 1). The results show that it is a reverse faulting at a depth of 13–15 km on a plane dipping 40–47° to N46°W. The 22 km centroid depth in GCMT is likely to be over-estimated, often found for events of this magnitude range in the GCMT catalog (Chu et al., 2009). The source duration of 4 s estimated in our study is noticeable shorter than the 10 s source duration based on finite source inversion using teleseismic body-wave waveforms (Zeng et al., 2013a; Liu et al., 2013). The discrepancy is probably due to the point-source approximation (Xie et al., 2013) and ignoring the rupture directivity effect. Future enhancements to gCAP3D includes adding a grid search for the rupture direction.

In summary, we have developed a new inversion method gCAP3D for determining general moment tensor of a seismic source using 3D Green's functions. It inherits the advantageous features of the "Cut-and-Paste" (CAP) method to break a full seismogram into the Pnl and surface-wave segments and to allow time shift between observed and predicted waveforms. It uses grid search for 5 source parameters (relative strengths of the isotropic and CLVD components and the strike, dip, and rake of the DC component) that minimize the waveform misfit. The scalar moment is estimated using the ratio of L_2 norms of the data and synthetics. We applied gCAP3D to the 2013 M_s 7.0 Lushan earthquake and its aftershocks using a 3D crustal-upper mantle velocity model derived from ambient noise tomography in the region. We first relocated the events using the double-difference method. We then used the finite-differences method and reciprocity principle to calculate Green's functions of the 3D model for 20 permanent broadband seismic sta-

tions within 200 km from the source region. We obtained moment tensors of the mainshock and 74 aftershocks ranging from M_w 5.2 to 3.4. The results show that the Lushan earthquake is a reverse faulting at a depth of 13–15 km on a plane dipping 40–47° to N46°W. Most of the aftershocks occurred off the main rupture plane and have similar focal mechanisms to the mainshock's, except in the proximity of the mainshock where the aftershocks' focal mechanisms display some variations.

Acknowledgments

References

Bevington, P.R., Robinson, D.K., 1992. Data reduction and error analysis for the physical sciences. McGraw-Hill, Inc.

Chapman, C.H., Leaney, W.S., 2012. A new moment-tensor decomposition for seismic events in anisotopic media. Geophys. J. Int. 188, 343–370. doi:10.1111/j.1365-246X.2011.05265.x.

Chen, W., Ni, S., Kanamori, H., Wei, S., Jia, Z., Zhu, L., 2015. CAPjoint, a computer software package for joint inversion of moderate earthquake

source parameters with local and teleseismic waveforms. Seismol. Res. Lett. 86, 432–441. doi:doi:10.1785/0220140167.

Chu, R., Zhu, L., Helmberger, D.V., 2009. Determination of earthquake focal depths and source time functions in central Asia using teleseismic P waveforms. Geophys. Res. Lett. 36, L17317, doi:10.1029/2009GL039494.

Covellone, B.M., Savage, B., 2012. A quantitative comparison between 1D and 3D source inversion methodologies: Application to the Middle East. Bull. Seismol. Soc. Am. 102, 2189–2199.

Dahlen, F.A., Tromp, J., 1998. Theoretical Global Seismology. Princeton University Press, Princeton, NJ.

Dreger, D.S., 2003. TDMT_INV: Time domain seismic moment tensor inversion. International Handbook of Earthquake and Engineering Seismology 81B, 1627.

Ekstrom, G., Nettles, M., Dziewonski, A.M., 2012. The global CMT project 2004–2010: Centroid-moment tensor for 13,017 earthquakes. Phys. Earth Planet. Inter. 200–201, 1–9. doi:10.1016/j.pepi.2012.04.002.

Graves, R., 1996. Simulating seismic wave propagation in 3D elastic media using staggered-grid finite differences. Bull. Seismol. Soc. Am. 86, 1091–1106.

Han, L., Zeng, X., Jiang, C., Ni, S., Zhang, H., Long, F., 2014. Focal mechanisms of the 2013 Mw6.6 Lushan, China earthquake and high-resolution aftershock relocations. Seismol. Res. Lett. 85, 8–14.

Hingee, M., Tkali, H., Fichtner, A., Sambridge, M., 2011. Seismic moment tensor inversion using a 3-D structural model: applications for the australian region. Geophys. J. Int. 184, 949–964. doi:10.1111/j.1365-246X.2010.04897.x.

Hjorleifsdottir, V., Ekstrom, G., 2010. Effects of three-dimensional Earth structure on CMT earthquake parameters. Phys. Earth Planet. Inter. 179, 178–190.

Julian, B.R., Miller, A.D., Foulger, G.R., 1998. Non-double-couple earthquakes: 1. theory. Rev. Geophys. 36, 525–549.

Kuhn, D., Vavrycuk, V., 2013. Determination of full moment tensors of microseismic events in a very heterogeneous mining environment. Tectonophysics 589, 33–43. doi:10.1016/j.tecto.2012.12.035.

Lin, X.D., Ge, H.K., Xu, P., Dreger, D., Su, J.R., Wang, B.S., Wu, M.J., 2013. Near-field full waveform inversion: Lushan magnitude 7.0 earthquake and its aftershock moment tensors (in Chinese with English abstract). Chinese J. Geophys. 56, 4037–4047. doi:10.6038/cjg20131209.

Liu, C., Zheng, Y., Ge, C., Xiong, X., Xu, H.Z., 2013. Rupture process of the 2013 M7.0 Lushan earthquake (in Chinese with English abstract). Science China: Earth Sciences doi:10.1007/s11430-013-4639-9.

Liu, Q., Polet, J., Komatisch, D., Tromp, J., 2004. Spectral-element moment tensor inversions for earthquakes in southern California. Bull. Seismol. Soc. Am. 94. doi:10.1785/012004038.

Lu, J., Wang, X., Su, J., Pan, L., 2013. Hypocentral location and source mechanism of the $M_s7.0$ Lushan earthquake sequence (in Chinese with English abstract). Chinese J. Geophys. 56, 1753–1763. doi:10.6038/cjg20130533.

Ramos-Martinez, J., McMechan, G.A., 2001. Source-parameter estimation by full waveform inversion in 3D heterogeneous, viscoelastic, anisotropic media. Bull. Seismol. Soc. Am. 91, 276–291.

Tan, Y., Helmberger, D., 2007. A new method for determining small earthquake source parameters using short-period P waves. Bull. Seismol. Soc. Am. 97, 1176–1195. doi:10.1785/0120060251.

Tan, Y., Zhu, L., Helmberger, D.V., Saikia, C.K., 2006. Locating and modeling regional earthquakes with two stations. J. Geophys. Res. 111, B01306, doi:10.1029/2005JB003775.

Tape, W., Tape, C., 2012. A geometric setting for moment tensors. Geophys. J. Int. 190, 476–498.

Vavrycuk, V., 2015. Moment tensor decompositions revisited. J. Seismol. 19, 231–252. doi:10.1007/s10950-014-9463-y.

Waldhauser, F., Ellsworth, W.L., 2000. A double-difference earthquake location algorithm: Method and application to the northern Hayward fault, California. Bull. Seismol. Soc. Am. 90, 1353–1368.

Xie, Z.J., Jin, B.K., Zheng, Y., Ge, C., Xiong, X., Xiong, C., Xu, H.Z., 2013. Source parameters inversion of the 2013 Lushan earthquake by combin-

ing teleseismic waveforms and local seismograms (in Chinese with English abstract). Science China: Earth Sciences doi:10.1007/s11430-013-4640-38.

Zeng, X., Luo, Y., Han, L., 2013a. Preliminary result for rupture process of Apr. 20, 2013, Lushan Earthquake, Sichuan, China (in Chinese with English abstract). Chinese J. Geophys. 56, 1418–1424.

Zeng, X., Luo, Y., Han, L., 2013b. The Lushan M7.0 earthquake on 20 April 2013: A high-angle thrust event (in Chinese with English abstract). Chinese J. Geophys. 56, 1418–1424.

Zhao, L., Chen, P., Jordan, T.H., 2006. Strain Greens tensors, reciprocity and their applications to seismic source and structure studies. Bull. Seismol. Soc. Am. 96, 1753–1763.

Zhao, L.S., Helmberger, D.V., 1994. Source estimation from broadband regional seismograms. Bull. Seismol. Soc. Am. 84, 91–104.

Zhao, Z., Fan, J., Zheng, S.H., 1997. Precision determination of the crustal structure and hypocentral locations in the longmenshan thrust nappe belt (in Chinese with English abstract). Chinese J. Geophys. 19, 615–622.

Zheng, X.F., Yao, Z.X., Liang, J.H., Zheng, J., 2010. The role played and opportunities provided by IGP DMC of China National Seismic Network in Wenchuan earthquake disaster relief and researches. Bull. Seismol. Soc. Am. 100, 2866–2872. doi:10.1785/0120090257.

Zheng, Y., Ge, C., Xie, Z.J., Yang, Y.J., Xiong, X., Xu, H.Z., 2013. Crustal and upper mantle structure and the deep seismogenic environment in the

source regions of the Lushan earthquake and the Wenchuan earthquake (in Chinese with English abstract). Science China: Earth Science 43. doi:10.1007/s11430-013-4641-2.

Zhu, L., Ben-Zion, Y., 2013. Parameterization of general seismic potency and moment tensors for source inversion of seismic waveform data. Geophys. J. Int. 194, 839–843. doi:10.1093/gji/ggt137.

Zhu, L., Helmberger, D.V., 1996. Advancement in source estimation techniques using broadband regional seismograms. Bull. Seismol. Soc. Am. 86, 1634–1641.

Zhu, L., Helmberger, D.V., Saikia, C.K., Woods, B.B., 1997. Regional waveform calibration in the Pamir-Hindu Kush region. J. Geophys. Res. 102, 22799–22813.

Zhu, L., Rivera, L.A., 2002. A note on the dynamic and static displacements from a point source in multi-layered media. Geophys. J. Int. 148, 619–627.

Zhu, L., Tan, Y., Helmberger, D.V., Saikia, C.K., 2006. Calibration of the Tibetan plateau using regional seismic waveforms. PAGEOPH 163, 1193–1213, doi:10.1007/s00024–006–0073–7.

Vs (km/s) at 5 km
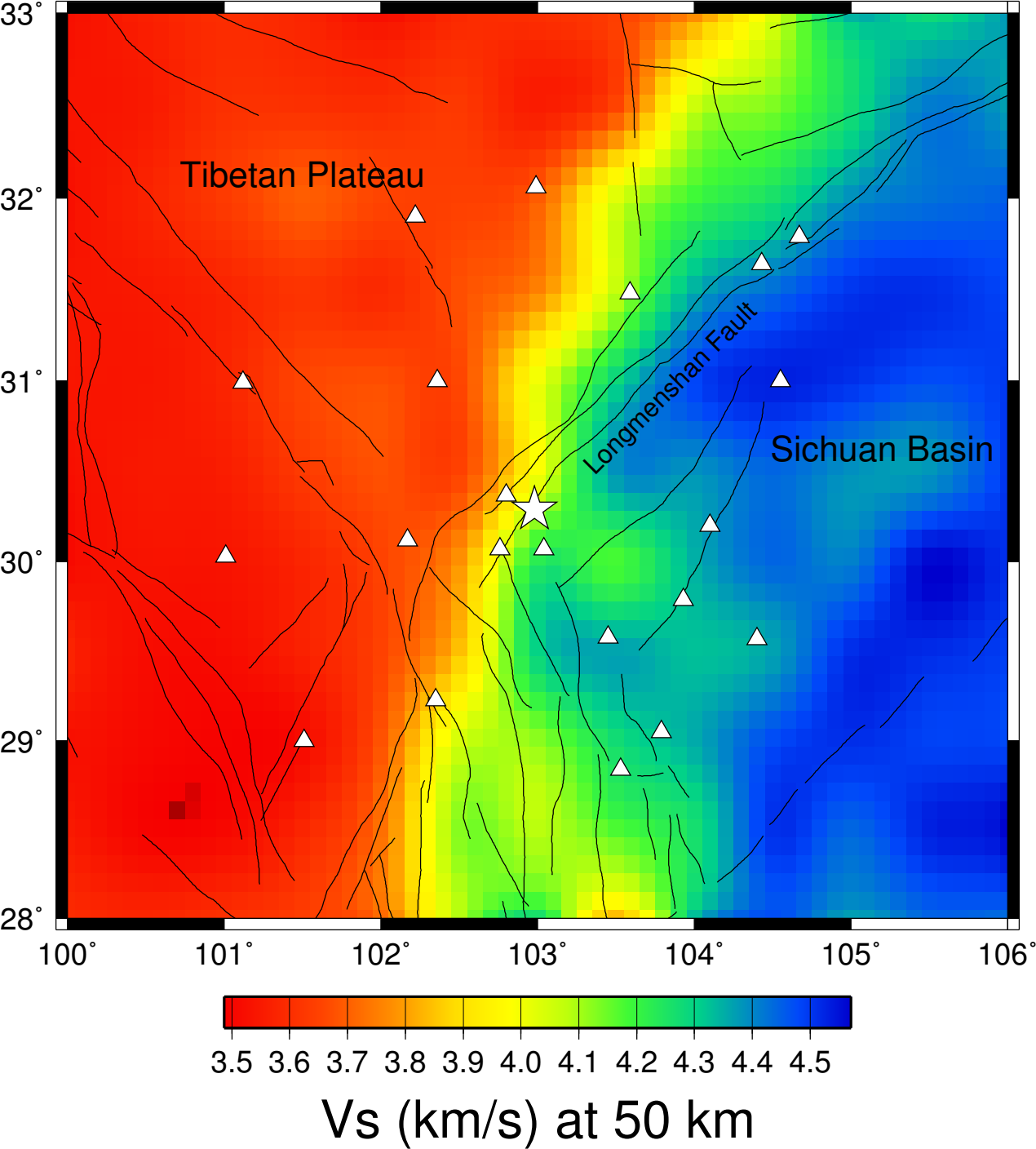
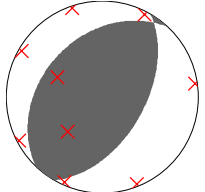Vs (km/s) at 10 km

Vs (km/s) at 20 km

Vs (km/s) at 50 km
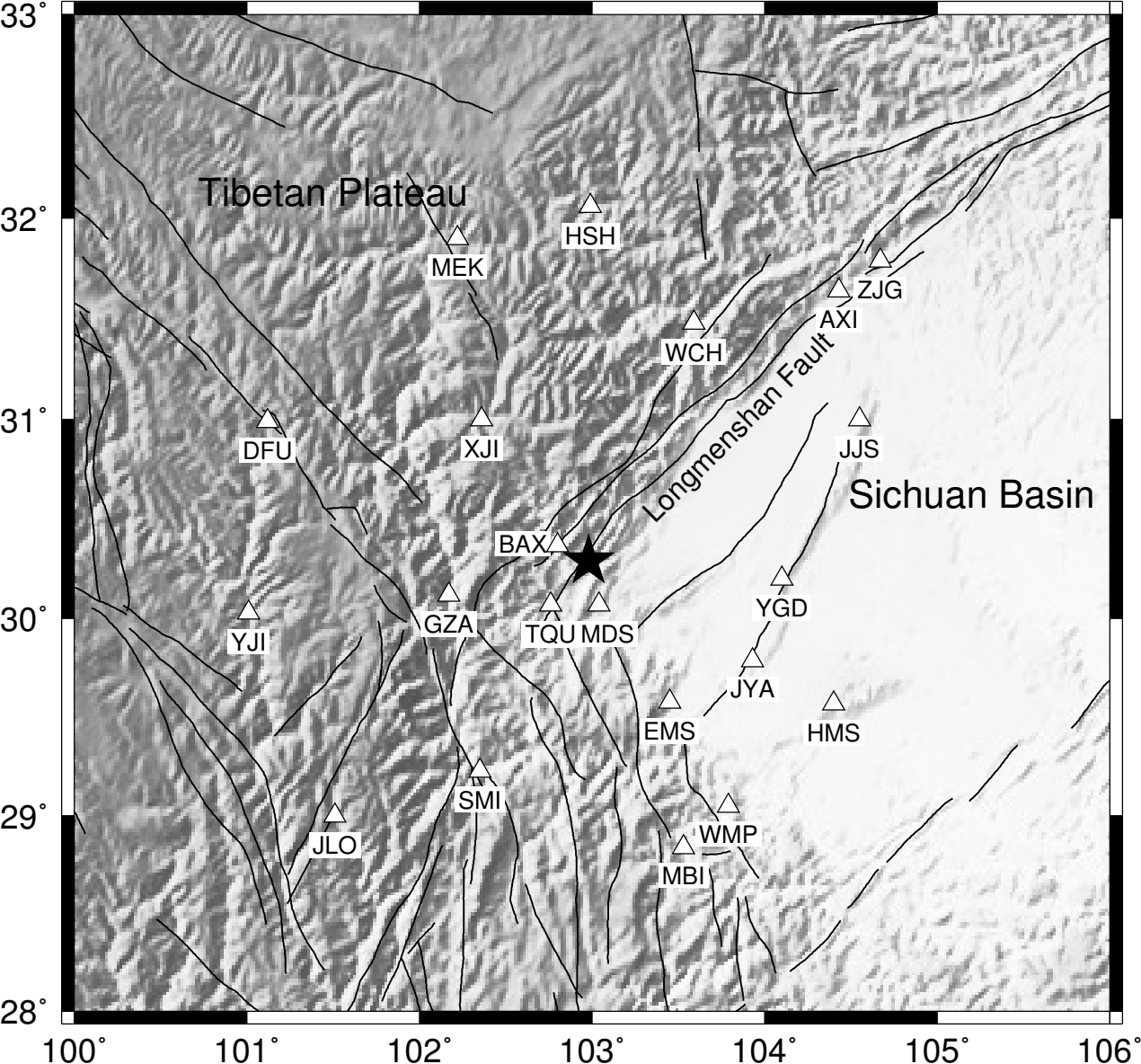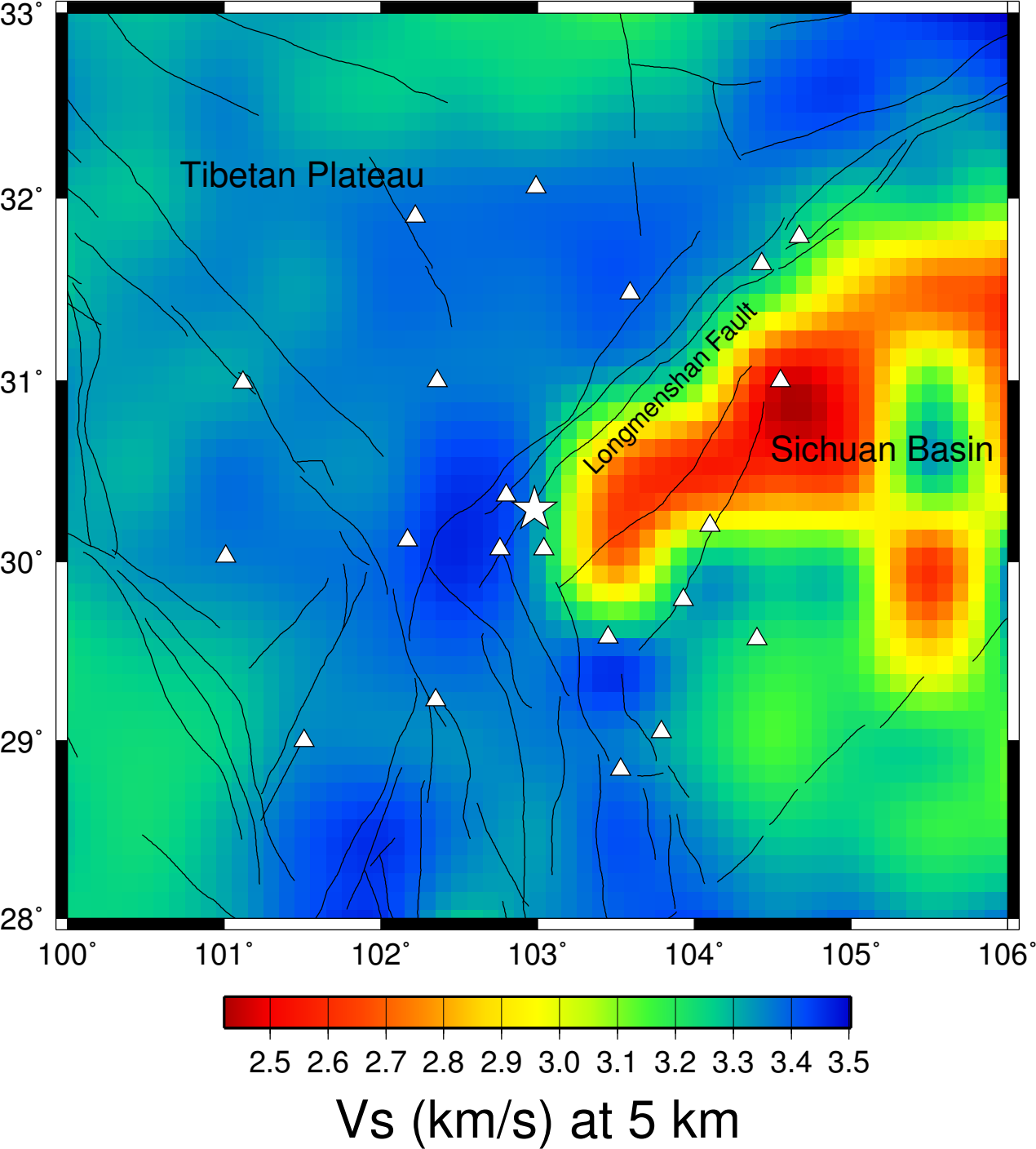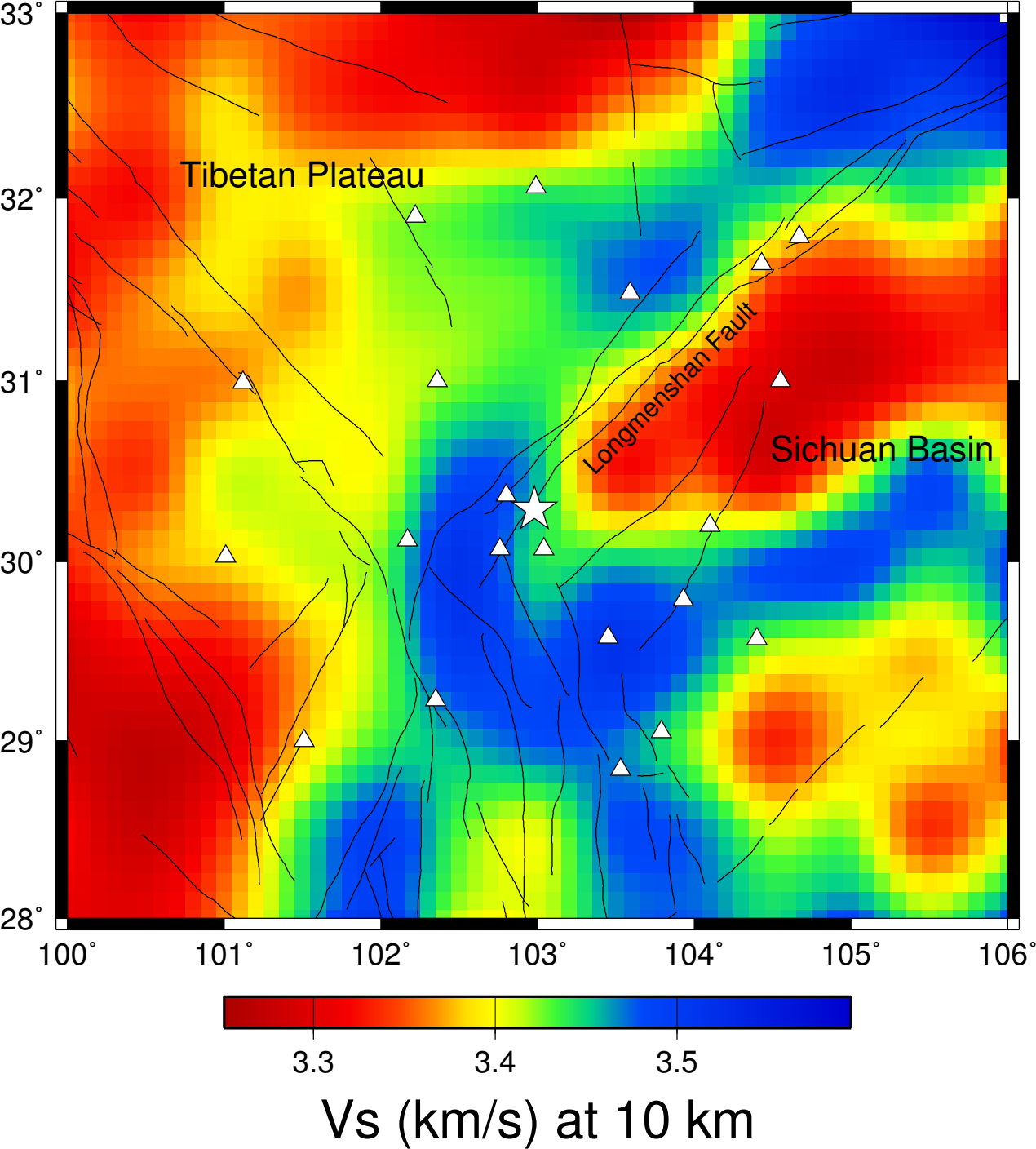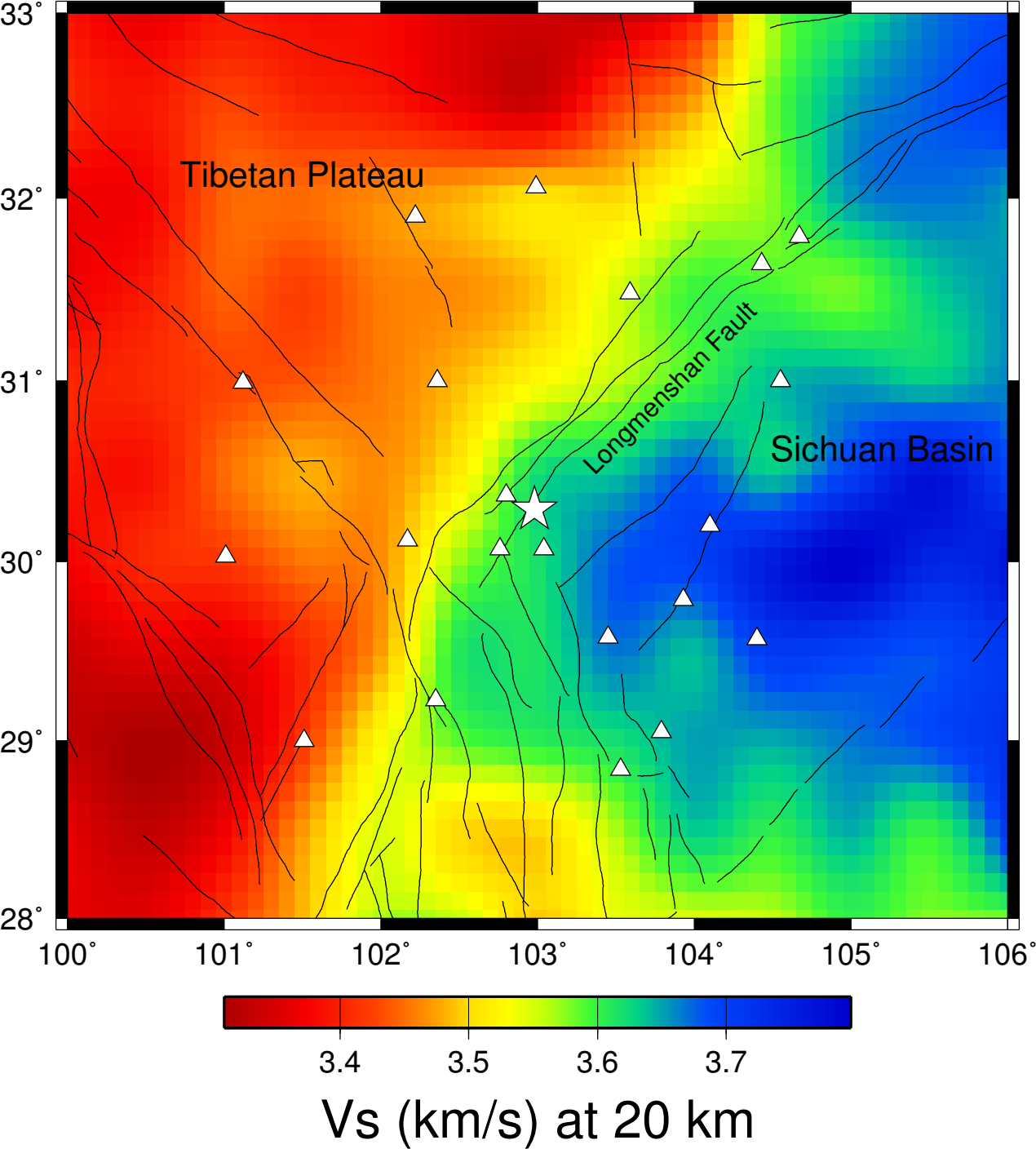
Event 20130420000246 Model and Depth 1D_15
FM 30 54 82 Mw 6.37 E 8.109e+01 589 ERR 2 4 6 ISO 0.00 0.00 CLVD 0.00 0.00
Variance reduction 64.0

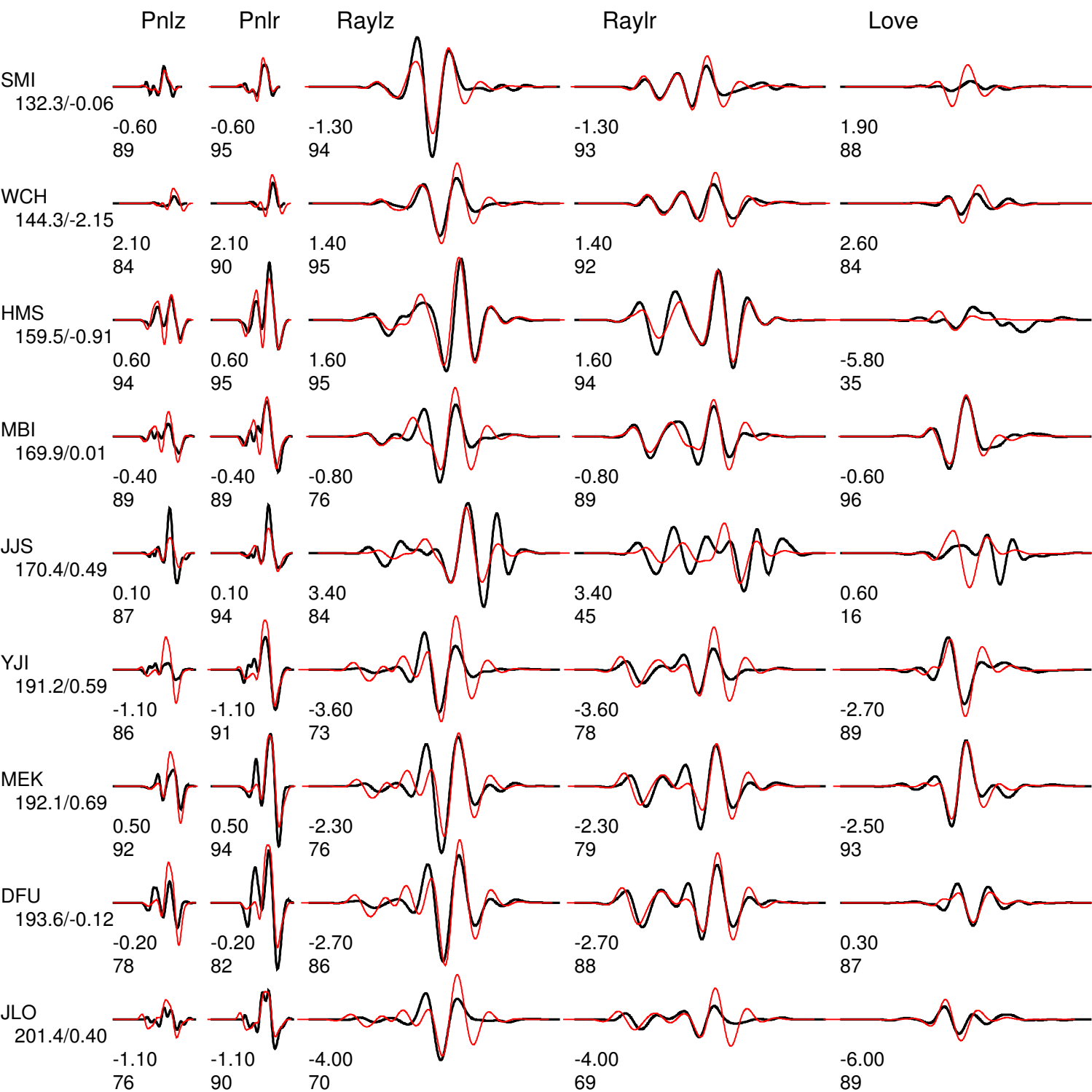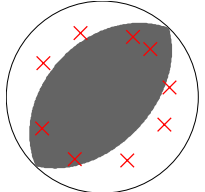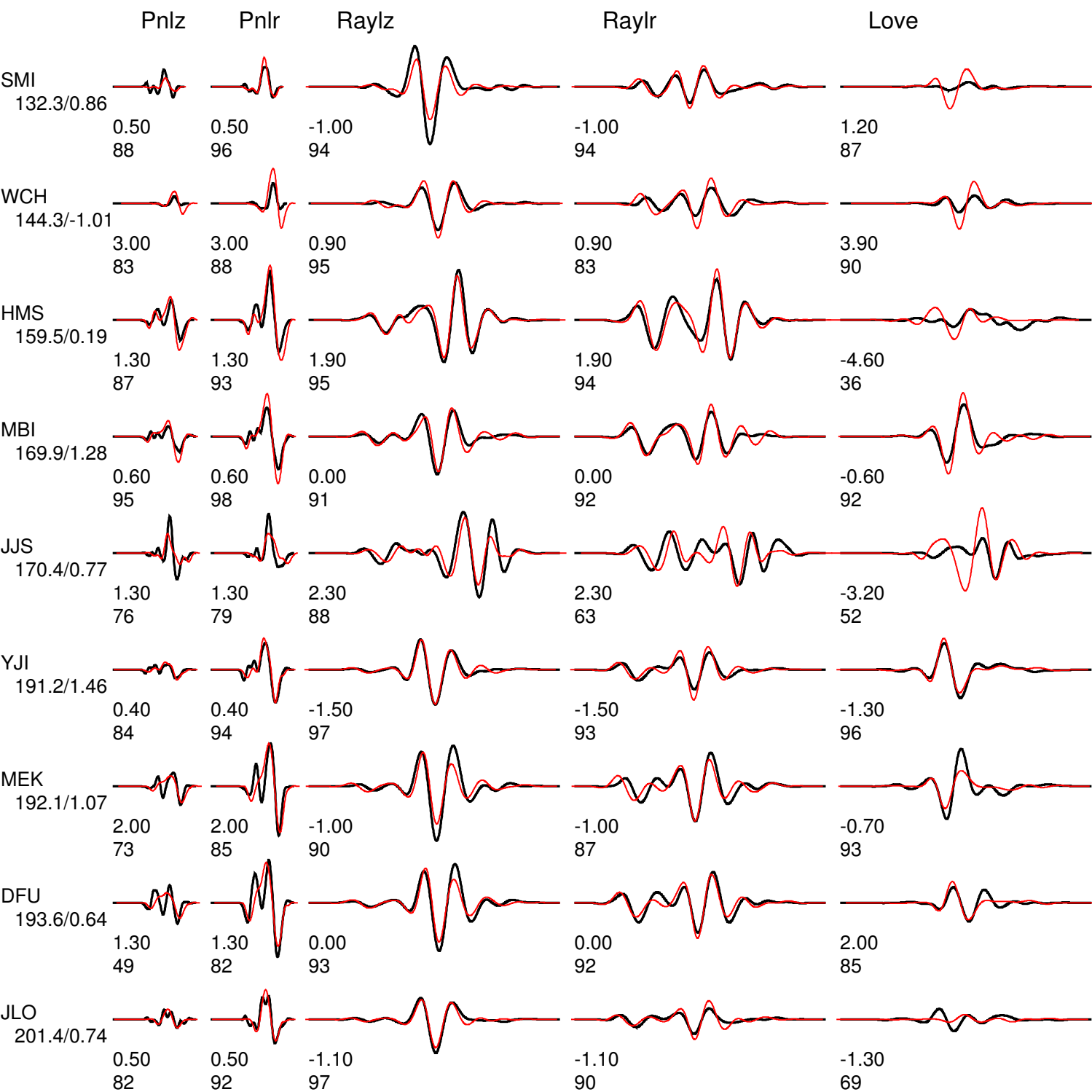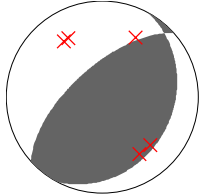|	Pnlz	Pnlr	Raylz	Raylr	Love
SMI 132.3/-0.06	-0.60 89	-0.60 95	-1.30 94	-1.30 93	1.90 88
WCH 144.3/-2.15	2.10 84	2.10 90	1.40 95	1.40 92	2.60 84
HMS 159.5/-0.91	0.60 94	0.60 95	1.60 95	1.60 94	-5.80 35
MBI 169.9/0.01	-0.40 89	-0.40 89	-0.80 76	-0.80 89	-0.60 96
JJS 170.4/0.49	0.10 87	0.10 94	3.40 84	3.40 45	0.60 16
YJI 191.2/0.59	-1.10 86	-1.10 91	-3.60 73	-3.60 78	-2.70 89
MEK 192.1/0.69	0.50 92	0.50 94	-2.30 76	-2.30 79	-2.50 93
DFU 193.6/-0.12	-0.20 78	-0.20 82	-2.70 86	-2.70 88	0.30 87
JLO 201.4/0.40	-1.10 76	-1.10 90	-4.00 70	-4.00 69	-6.00 89

50 s

Event 20130420000246 Model and Depth 3D_fix
FM 224 41 90 Mw 6.53 E 7.245e+01 590 ERR 2 4 6 ISO 0.00 0.00 CLVD 0.00 0.00
Variance reduction 68.3

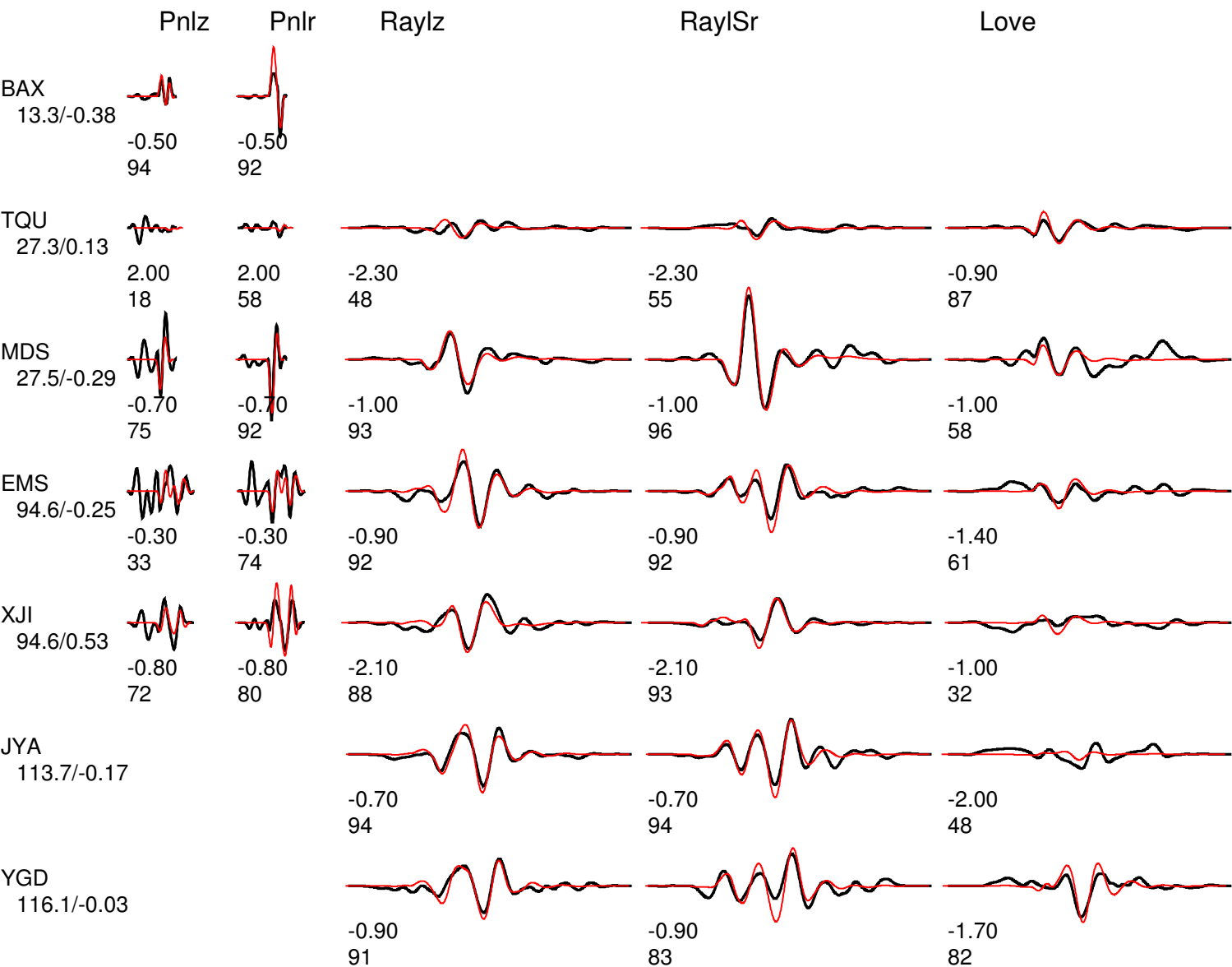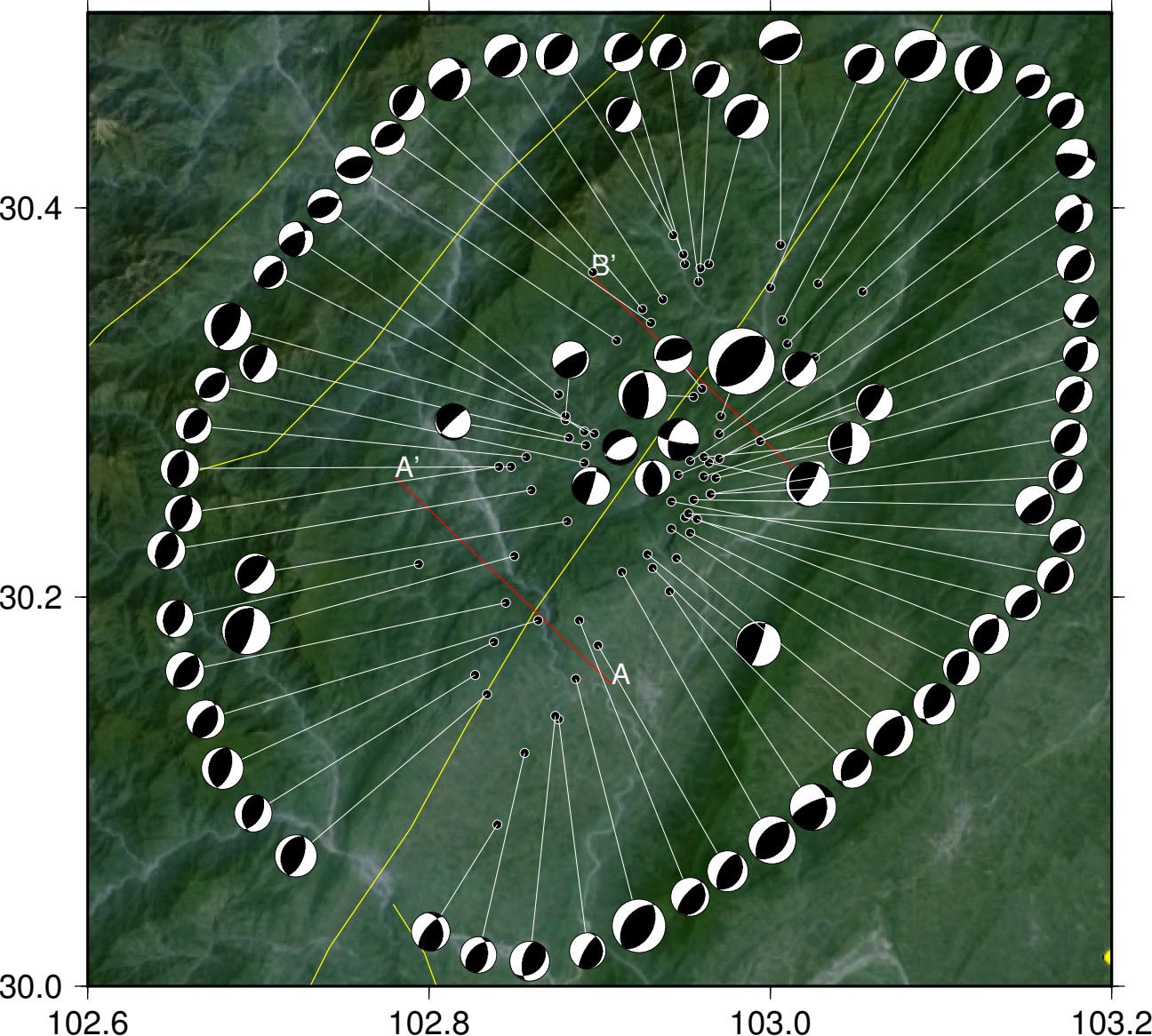|	Pnlz	Pnlr	Raylz	Raylr	Love
SMI 132.3/0.86	0.50 88	0.50 96	-1.00 94	-1.00 94	1.20 87
WCH 144.3/-1.01	3.00 83	3.00 88	0.90 95	0.90 83	3.90 90
HMS 159.5/0.19	1.30 87	1.30 93	1.90 95	1.90 94	-4.60 36
MBI 169.9/1.28	0.60 95	0.60 98	0.00 91	0.00 92	-0.60 92
JJS 170.4/0.77	1.30 76	1.30 79	2.30 88	2.30 63	-3.20 52
YJI 191.2/1.46	0.40 84	0.40 94	-1.50 97	-1.50 93	-1.30 96
MEK 192.1/1.07	2.00 73	2.00 85	-1.00 90	-1.00 87	-0.70 93
DFU 193.6/0.64	1.30 49	1.30 82	0.00 93	0.00 92	2.00 85
JLO 201.4/0.74	0.50 82	0.50 92	-1.10 97	-1.10 90	-1.30 69

50 s

Event 20130424133635 Model and Depth 3D_fix

FM 28 27 72 Mw 3.36 E 4.584e-08 433 ERR 2 4 10 ISO 0.00 0.00 CLVD 0.00 0.00

Variance reduction 84.1

	Pnlz	Pnlr	Raylz	RaylSr	Love
BAX 13.3/-0.38	-0.50 94	-0.50 92			
TQU 27.3/0.13	2.00 18	2.00 58	-2.30 48	-2.30 55	-0.90 87
MDS 27.5/-0.29	-0.70 75	-0.70 92	-1.00 93	-1.00 96	-1.00 58
EMS 94.6/-0.25	-0.30 33	-0.30 74	-0.90 92	-0.90 92	-1.40 61
XJI 94.6/0.53	-0.80 72	-0.80 80	-2.10 88	-2.10 93	-1.00 32
JYA 113.7/-0.17			-0.70 94	-0.70 94	-2.00 48
YGD 116.1/-0.03			-0.90 91	-0.90 83	-1.70 82

50 s